

## **EXPERIMENTAL AND NUMERICAL INVESTIGATION OF THE COOLING AIR FLOW IN AN ELECTRIC GENERATOR**

Moradnia P.\*, Chernoray V. and Nilsson H.

\*Author for correspondence

Department of Applied Mechanics,  
Chalmers University of Technology,  
412 96, Gothenburg,  
Sweden,

E-mail: [pirooz.moradnia@chalmers.se](mailto:pirooz.moradnia@chalmers.se)

### **ABSTRACT**

The cooling air flow in a small-scale electric generator has been investigated experimentally and numerically, and the results have been compared to each other. The studies have been made in cold conditions, without heat transfer. The velocity profiles at the inlet of the generator have been measured by means of a 5-hole probe, traversed in the axial direction to give the axial distribution of the radial velocities at the inlet of the generator. The outlet velocity distribution has been measured by means of a total-pressure rake, consisting of a number of total pressure probes, which gives the horizontal distribution of the velocity magnitudes, aligned with the stator channels at the outlet of the generator. Smoke visualization of the flow has been performed at the inlet of the generator and the flow pattern has been visualized.

The numerical study has been performed using the OpenFOAM open source CFD software. The corresponding numerical velocity profiles at the inlet and the outlet of the generator have been extracted and compared with the experimental profiles. The velocity vectors at the inlet of the generator have been compared to the flow pattern obtained by the smoke visualization.

Because of geometrical dissimilarities between the experimental rig and the numerical computational domain, there are unavoidable differences in the results. This yields a qualitative comparison, although the comparisons still show a relatively good quantitative agreement between the experiments and the numerical simulations.

### **INTRODUCTION**

Studies of the cooling air flow in generators is of high importance. Sufficient and correct cooling in generators lead to longer lifetimes of certain components, such as insulation. Furthermore, the electric resistances of the coils and the windings are temperature dependent, which means that in order to keep the generator at its highest efficiency, it should work in

a certain design temperature range. The air flow itself also contributes to a significant part of the total efficiency reduction, and there is room for improvement from a fluid dynamics point of view. A good knowledge of the air flow in the generators is therefore essential to have a high energy conversion efficiency. In previous computational studies by Moradnia et al. [1,2] the effect of different rotor and stator designs on the flow characteristics in a generator has been parametrically studied. In the study by Houde et al. [3], the cooling air flow in a radially cooled generator has been numerically and experimentally investigated.

In the present work the air flow in a small axially cooled generator has been investigated experimentally and numerically as a first step to further increase the knowledge of the air cooling processes.

### **NOMENCLATURE**

$G$	$[\text{m}^2/\text{s}^3]$	Production rate of the turbulent kinetic energy
$K$	$[\text{m}^2/\text{s}^2]$	Turbulent kinetic Energy
$P$	[pa]	Pressure
$U$	[m/s]	Velocity
Special characters		
$\varepsilon$	$[\text{m}^2/\text{s}^3]$	Decay rate of the turbulent kinetic energy
$\nabla$	[-]	Gradient
$\Omega$	[rad/s]	Rotational speed of the rotating reference frame
$\rho$	$[\text{kg}/\text{m}^3]$	Density
$\nu$	$[\text{m}^2/\text{s}]$	Kinematic viscosity of the fluid
Subscripts		
$dyn$		Dynamic
$I$		Inertial reference frame
$r$		Rotational reference frame
$stat$		Static
$t$		Turbulent
$tot$		Total

## EXPERIMENTAL RIG

The generator studied in this work is located at Uppsala University in Uppsala city, Sweden. Figure 1 shows the generator rig with its main components during the installation. The generator has a casing with 12 openings (windows). The casing is located outside the stator and is connected to the supporting frame. Out of the 12 casing windows there are only 7 available for measurements, while the rest 5 are blocked by the frame mountings.



**Figure 1:** The generator rig used in the experimental measurements, with its main components

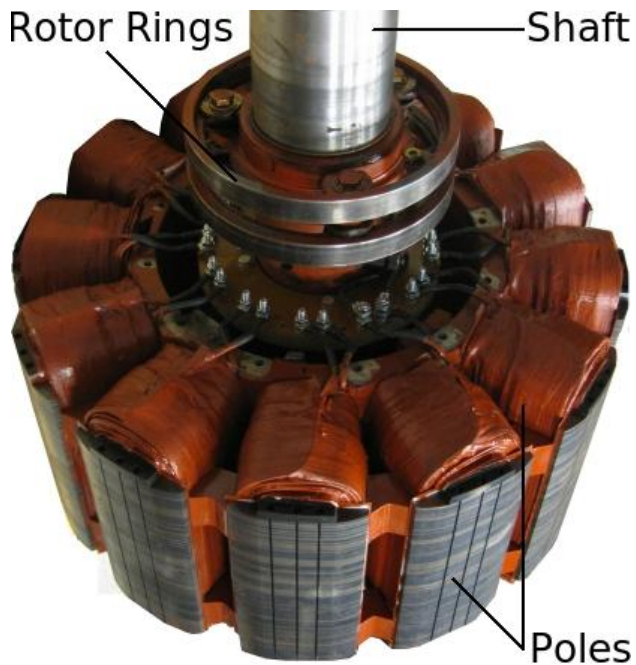


**Figure 2:** The rotor used in the present study

A generator is made up of two main components: a rotor and a stator. The present rotor, shown in Figures 2 and 3, has 12 electromagnetic poles, is located inside the stator and rotates with a rotational speed of 500 rpm. The outer radius of the rotor is 356 mm. Over the space between each two adjacent rotor poles a flat rectangular fan blade is installed. Above the rotor poles and on the shaft, there are two slip ring collectors, which under the experiments were sealed by tape to form a single cylinder.

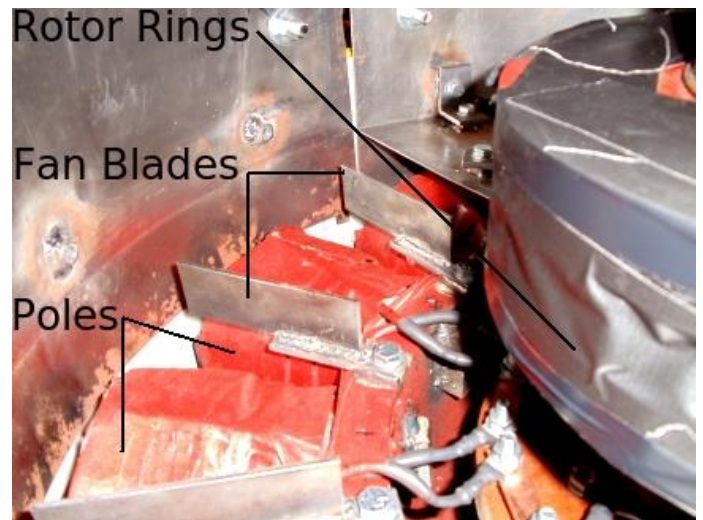


**Figure 3:** The geometrical details of the rotor

The present stator has an inner and an outer radius of 365 mm and 438 mm respectively. In the stator there are four rows of cooling channels, each of which consists of 108 cooling channels, leading to a total of 432 cooling channels in the stator.

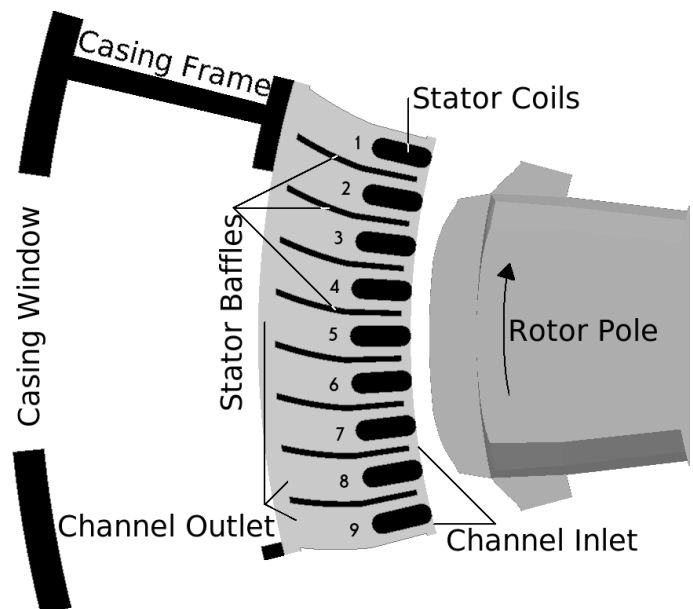


**Figure 4:** The stator cooling channels with their respective numbers as well as stator coils. The direction of rotation for the rotor is shown with a curved arrow on the pole.

Figure 4 shows a cross-section of a set of stator cooling channels as well as the position of the stator coils within the channels. A cooling channel is identified by the open space between the stator plates on top and bottom, as well as thin baffles on the sides, which separate the two adjacent channels. The cooling channels surround the stator coils.

In the tangential direction there are 9 cooling channels per window in each channel row. Since the casing is mounted on the outer surface of the stator, some flow blockage occurs just at the outlet of certain stator channels, which is caused by the casing frame. Only 6 channels per window are fully open at the outlet in the tangential direction, as shown in Figure 4.

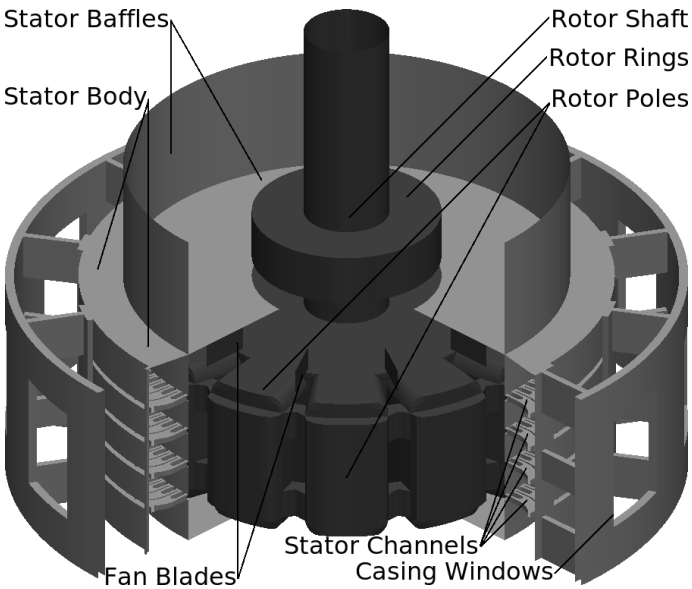


**Figure 5:** Generator parts. The front part of the geometry has been taken away for better visibility.

Figure 5 shows a schematic drawing of the generator parts. The stator has a set of horizontal and vertical baffles to confine the inlet area and to have a more deterministic flow at the inlet. A thin baffle has also been attached to the bottom part of the rotor shaft to completely block the flow from below. This would eliminate the eventual flow unbalances which may be caused by unequal flow distributions between the original two inlets to the generator by reducing them to only one at the top.

## MEASUREMENTS

The experimental part of this work consists of flow measurements at the inlet and outlet of the generator and smoke visualizations. The flow visualizations were performed by so-called smoke pens which are normally used for the monitoring of ventilation systems. The smoke pens are compact in size and produce highly intensive and thin smoke streaks. During the visualizations the pens were placed at different axial, radial and tangential positions at the inlet of the generator to monitor the flow streamlines. The flow visualizations demonstrated that the inlet flow was turbulent and axi-symmetric.



**Figure 6:** The 5-hole probe used in the measurements

The flow measurements at the inlet were performed by a five-hole pressure probe. The probe is of L-type with a tip diameter of 1.6 mm, see Figure. 6. The probe was calibrated for the cone angles from 0 to 52 degrees. To spatially position the probe at the generator inlet a two-axial traversing system was used. The traversing system movement is controlled by stepper motors with a resolution of better than 2  $\mu\text{m}$ . A dedicated PC was used to control the motion of the traversing system. The precision of the measurements by the 5-hole probe is predominantly defined by the initial positioning of the probe in the facility. The tolerance of the initial positioning of the probe was 0.1 mm in the axial direction, 1 mm in the radial direction and  $\pm 1$  degree in the angular direction.

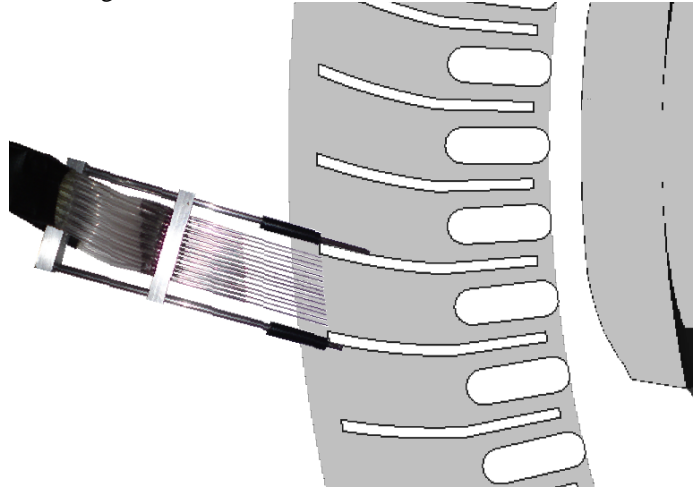


**Figure 7:** The total pressure rake and its position relative to the stator channels. A small part of the rotor is seen in the picture.

The outlet flow measurements were performed by a specially designed rake of total pressure probes. The rake is comprised of 15 total pressure tubes which were mounted in a holder. The rake holder is specifically shaped in a way that the rake was precisely positioned just at the outlet of the stator channel and along the channel centre plane. Figure 7 shows the total-pressure rake inserted into the stator cooling channel for the measurements. The rake tubes are positioned along the flow to maintain the best accuracy of the total pressure measurements (as known for best accuracy the incoming flow angle should be within 10 degrees). The positioning of the rake was performed manually and the rake was moved from channel to channel to monitor the outlet flow of 138 stators channels. The rest of the 432 channels were not accessible physically. From the total pressure the outlet velocity magnitude was computed for each rake channel as:

$$|u| = \sqrt{2(P_{tot} - P_{stat}) / \rho} \quad (1)$$

In this case the static pressure was assumed as constant and equal to the ambient pressure in the laboratory.

The pressures from the five-hole probe and the total pressure rake were monitored using a 16-channel PSI 9116 digital pressure scanner (Pressure Systems Inc.). The measuring range of the scanner transducers is  $\pm 2500$  Pa and the channel scanning frequency is 500 Hz. To maintain the highest possible accuracy in a low-pressure range the pressure transducers were regularly controlled for an offset and nulled before each set of measurements. The resulting precision of the transducer offset was better than 0.2 Pa which is also defining the measurement accuracy. The time-mean statistics was evaluated from 1000 samples for each channel in case of the total pressure rake, and from 2000 samples per channel in case of the five-hole probe. Thus, under the acquisition time intervals the rotor was performing 16 or 33 revolutions respectively.

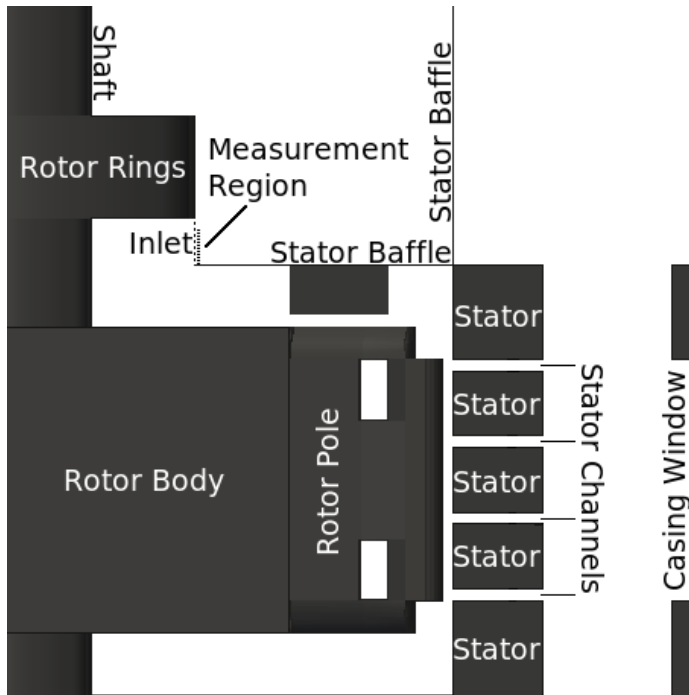


**Figure 8:** The schematic of the generator and the position of the inlet as well as the line where the inlet measurements were performed.

Figure 8 shows the schematic of the generator. The inlet is defined as the vertical cylindrical surface between the stator baffle and the rotor rings and shown by a dashed line. The 5-hole probe was positioned along the radial direction with the probe head 19 mm from the inlet as shown by the dotted line in Figure 8. The flow angle has a large variation just at the inlet to the generator. Due to restriction of the maximum probe measuring angle to 52 degrees the inlet flow was not resolved at all height of the inlet plane. The measurement data were not obtained for positions higher than 29 mm from the horizontal stator baffle as shown by the extent of the dashed line in Figure 8.

## NUMERICAL ANALYSIS

Figure 9 shows the computational domain used in the CFD computations with the imprints of the rotor, the stator and the surrounding boundaries. The computational domain has been made using a fully parameterized m4 script, which evaluates the geometrical parameters and writes them into an input file for the built-in OpenFOAM mesh generator named blockMesh. Due to periodicity only 1/12 of the generator is computed. The computational domain includes, thus, one rotor pole, 4 stator channel rows and 9 channels per channel row. The casing around the stator, the shaft rings, the rotor fan blades and the stator and rotor baffles have also been included in the geometry.

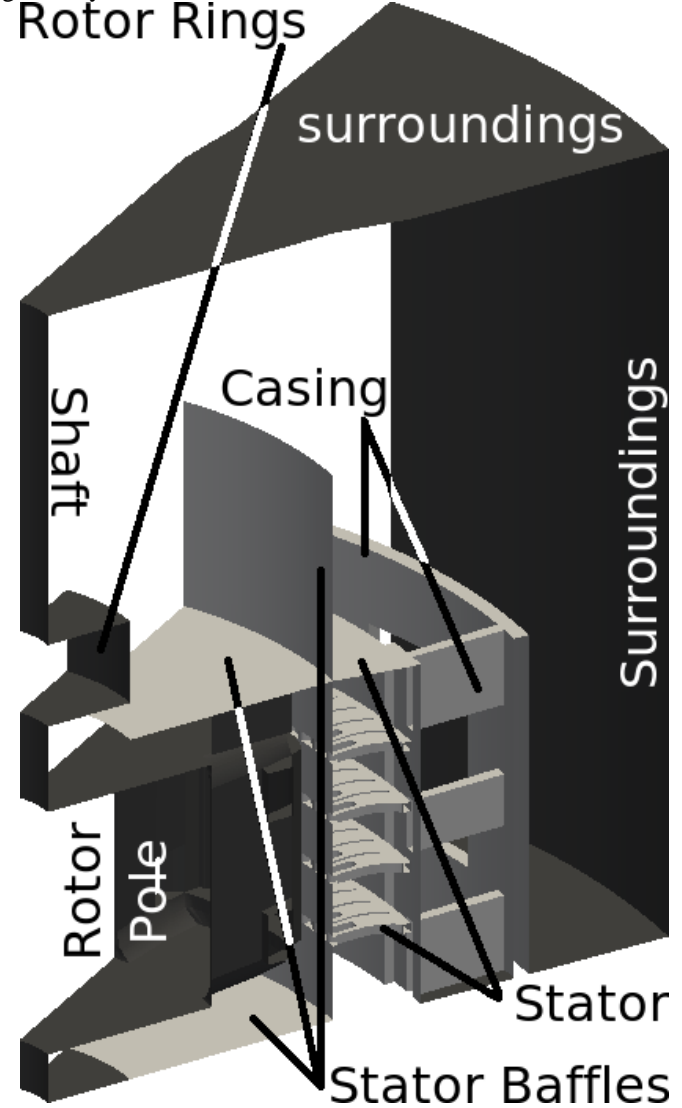


**Figure 9:** Computational domain excluding the cyclic boundaries

There are no inlet or outlet boundaries provided in the computational domain. Instead, the computational domain is extended both radially and axially outside, as well as above the stator to allow for an air recirculation in the domain. There is, thus, no prescribed volume flow in the case setup, but it is obtained by the solution. The cyclic boundaries at the two sides

of the computational domain are not visualized. The computational mesh consists of 17.5 million cells and the  $y^+$  values near the rotor and the stator walls, as well as inside the stator cooling channels are kept around 5.

The computations were performed using the MRFSimpleFOAM solver of the OpenFOAM-1.5.x open-source CFD toolbox.

The steady state solver is based on the frozen-rotor concept [4] where source terms for rotation are added in the rotating region and the relative positions between the rotating and stationary parts are fixed. The Navier-Stokes and continuity equations are based on convection of the absolute velocity  $\vec{U}_1$  and are given by

$$\nabla \cdot (\vec{U}_R \otimes \vec{U}_I) + \vec{\Omega} \times \vec{U}_I = -\nabla \left( \frac{P}{\rho} \right) + \nu \nabla \nabla \vec{U}_I \quad (2)$$

$$\nabla \cdot \vec{U}_I = 0$$

where  $\vec{U}_R$  is the velocity relative to each reference frame and  $\vec{\Omega}$  is the rotation vector of the reference frame. The rotating parts are coupled to the non-rotating parts at an axi-symmetric interface between the two regions.

The turbulence is modelled using the low-Re Launder-Sharma  $k-\varepsilon$  model [5], where the  $k$  and  $\varepsilon$  equations are defined as

$$\nabla \cdot (\vec{U} \tilde{k}) - \nabla D_{k,eff} \nabla k = G - \left( \tilde{\varepsilon} + D \right) \quad (3)$$

$$\nabla \cdot (\vec{U} \tilde{\varepsilon}) - \nabla D_{\varepsilon,eff} \nabla \tilde{\varepsilon} = C_{\varepsilon 1} G \frac{\tilde{\varepsilon}}{k} - f_2 C_{\varepsilon 2} \frac{\tilde{\varepsilon}}{k} + E$$

and the model coefficients are defined as

$D_{k,eff}$	$D_{\varepsilon,eff}$	$G$
$\nu + \frac{\nu_t}{\sigma_k}$	$\nu + \frac{\nu_t}{\sigma_\varepsilon}$	$2\nu_t S_{ij}^2$
$\nu_t$	$S_{ij}$	$\tilde{\varepsilon}$
$C_\mu f_\mu \frac{k^2}{\varepsilon}$	$\frac{1}{2} [U_{i,j} + U_{j,i}]$	$\varepsilon - D$
$D$	$E$	$f_\mu$
$2\nu  \nabla \sqrt{k} ^2$	$2\nu \nu_t  \nabla \nabla \vec{U} ^2$	$e^{\left( \frac{-3.4}{1 + \frac{k^2}{50\nu\varepsilon}} \right)^2}$
$f_2$	$\sigma_k$	$\sigma_k$
$1 - 0.3e^{-\min\left(\left(\frac{k^2}{\nu\varepsilon}\right)^2, 50\right)}$	1	1.3
$C_{\varepsilon 1}$	$C_{\varepsilon 2}$	$C_\mu$
1.44	1.92	0.09

The turbulence equations are solved using a first-order upwind differencing scheme. The velocity equations are solved using a blend of upwind and central differencing schemes called the Gamma scheme, which is second order accurate.

## RESULTS

The smoke visualizations show, see Figure 10, that the flow has a negligible tangential component at the inlet. It is purely radial just at the horizontal stator baffles and as one moves upwards from the horizontal baffles, an axial component gradually grows while the radial component weakens. Just at the rotor rings the radial velocity components have completely vanished and the flow is purely axial into the generator.

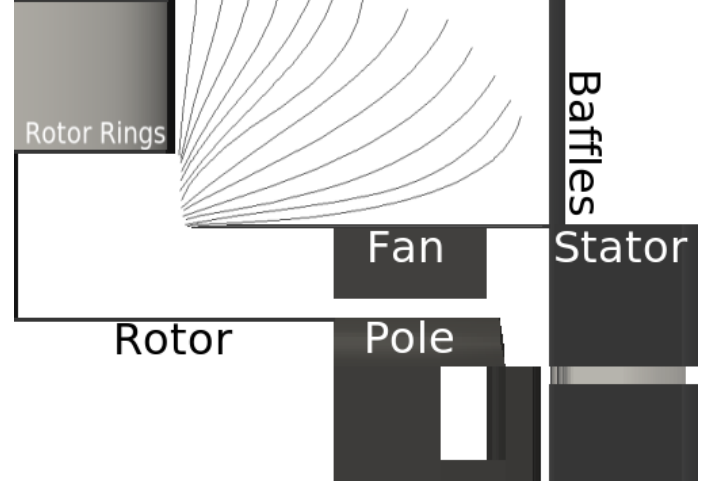


Figure 10: Schematic side view of the experimentally visualised streamlines at the inlet

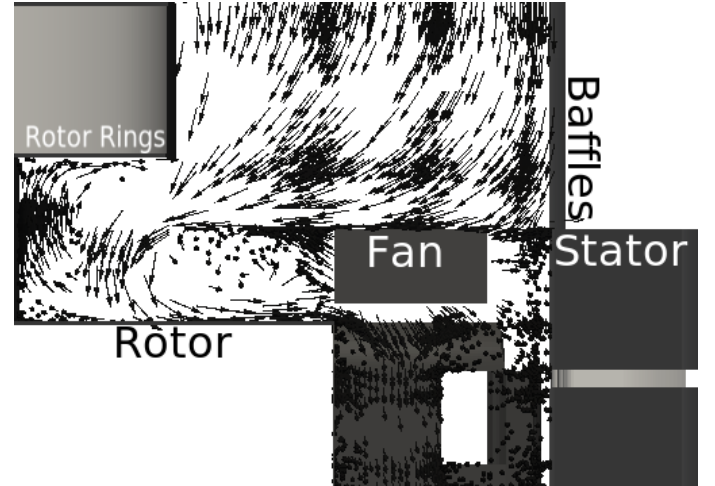
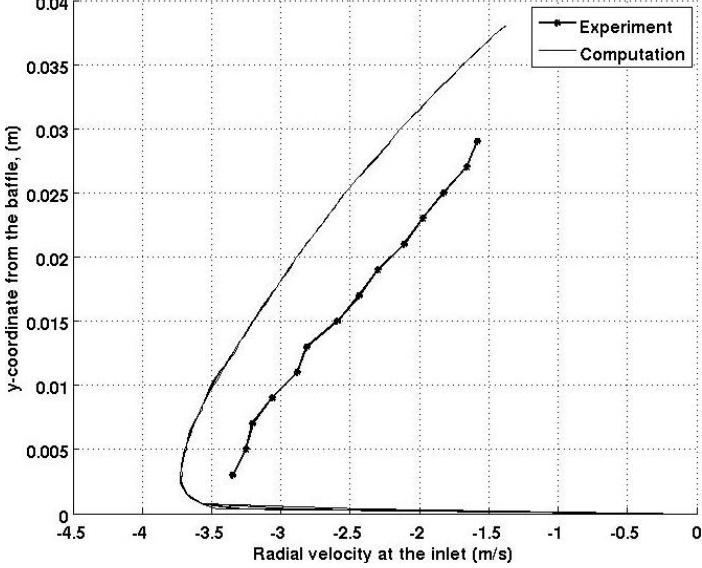


Figure 11: A side view of the numerically computed unit vectors of the flow at the inlet

Figure 11 shows the numerical visualization of the flow unit vectors at the same location as in Figure 10. The numerical results confirm the experimental observations. The flow has a negligible tangential component at the inlet and is purely radial at the stator baffles, which gradually transfers into purely axial towards the rotor rings.

Figure 12 shows the axial distribution of the radial velocity at the inlet, which has been experimentally measured along the inlet section shown in Figure 8. The axial distribution of the radial velocity along 7 different vertical sections has been investigated in the numerical case. The vertical sections have the same radial and axial positions as in the experiments, and each of them is located at a different tangential position in the computational domain. The radial distributions of velocity prove to be independent of the tangential position of the sections, which means that the radial velocity distribution in the numerical case is purely axi-symmetric.



**Figure 12:** The axial distributions of the numerical and experimental radial velocity at the inlet. From the numerical results the radial velocity at 7 different tangential positions are shown, proving a fully axi-symmetric flow

The experimental distribution of radial velocity shows the same behaviour as the numerical results but with smaller values. This may be related to a considerably larger outlet blockage in the experiments than in the simulations, yielding a smaller flow in the experimental case. Although the numerical model is highly detailed, there are many missing geometrical features.

The numerically obtained volume flow of the air through the computational domain is found to be

$$V_{num} = 0.158(m^3/s).$$

The experimental volume flow at the inlet is here roughly estimated as

$$V_{in,exp} = 2\pi rhU_r \approx 0.085 \left( \frac{m^3}{s} \right) \quad (4)$$

where  $V_{in,exp}$  is the volume flow based on the experiments at the inlet,  $r$  is the radius at which the probe tip is located (0.17m),  $h$  is the inlet height (0.038m) and  $U_r$  is the mean radial velocity along the vertical line at the inlet ( $\approx 2.1m/s$ ). The difference between the two volume flows can, as mentioned

before, be caused by the difference in blockages in the numerical and experimental cases.

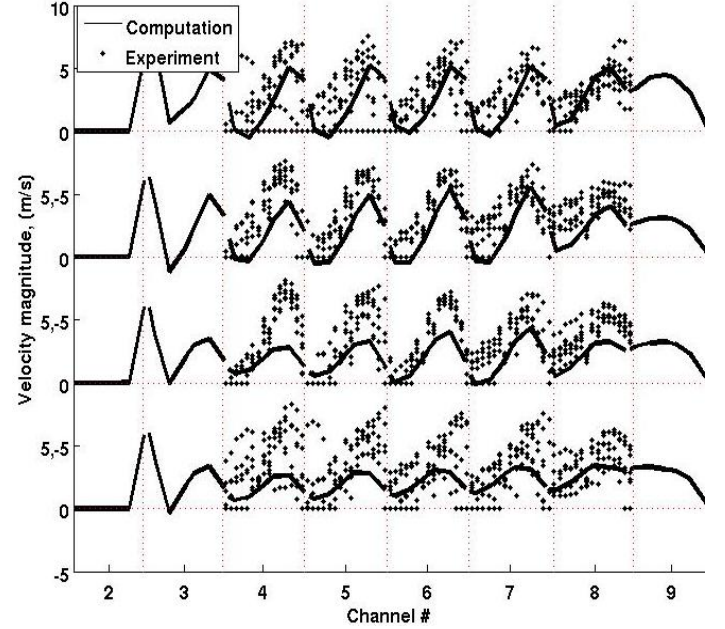


**Figure 13:** The numerical and experimental distributions of the velocity magnitudes at the stator channel outlets.

The experimental and numerical velocity distributions at the outlet of the stator channels are shown in Figure 13. The plot consists of the velocity distributions for four different channel rows, from lower to upper row. The horizontal axis shows the channel numbers, defined in Figure 4, while the vertical axis shows the velocities corresponding to each channel row. The solid curves show the numerical results, while the dots show the experimental values. The experimental results for all available casing windows are plotted. The scattering of the experimental results means that the velocity distributions for the channels in the same position in different casing windows are different. This can be interpreted as a non-periodicity at the outlet of the stator. The non-periodicity of the results can be explained by noticing the non-periodicity in the geometry. As Figure 4 suggests, the whole first channel as well as a large part of the second and the ninth channels are blocked by the geometry. Channels 3, 4 and 5 in one window are also blocked by the instrumentation. The third channel in each row is non-blocked, but impossible to access with the rake in the experiments, and this explains why the experimental data is shown only for channels 4 to 8 in each row. The numerically simulated flow pattern at the channel outlets is more similar to the measurements in the two top channel rows, while the consistency between the numerical results and the measurements is less in the two lower channel rows. The experimental volume flow at the outlet can be approximated by summing up the volume flows at all channel outlets. As Figure 13 shows, the velocity distributions in 5 channels are measured in the middle height of each channel row for the 7 open casing windows. According to Figure 4, out of 9 channels per row in each window, almost 2.5 channels are blocked at the outlet, which means 6.5 channels remain open at

the outlet. The average measured velocity magnitude at the centreline of the outlet of all measured channels is

$$U_{ave,cl} = 3.3 \text{ m/s}$$

The outlet velocity distributions in the vertical direction are not perfectly uniform, as the velocity approaches zero near the wall, which leads to a distribution of the velocities in the vertical direction. This means that the mean velocity magnitude over the outlet area should be lower than the mean velocity just at the centreline of the channels at the outlet. Considering the variations of the velocity profiles in the vertical direction, the area-weighted average velocity for the measured channels may be approximated as

$$U_{ave} \approx 0.85 * U_{ave,cl} = 2.8(\text{m/s})$$

Neglecting the recirculation regions, where the velocities are relatively small, the velocity vectors at the channel outlets can be assumed parallel with the channel walls. As the channel walls make an angle of  $\theta \approx 20^\circ$  with the radial direction, the average velocity for each channel should be projected in the radial direction as

$$U_{ave,rad} = U_{ave} * \cos(20^\circ) \approx 2.6(\text{m/s})$$

The average radial velocity should then be multiplied by the channel area just at the outlet

$$A_{ch} = 0.0094\text{m} * 0.02\text{m} \approx 1.9 * 10^{-4} \text{ m}^2$$

to give the volume flow for each channel. Assuming the same average velocity for the unmeasured channels (6.5 open channels per row in each window, 4 rows and 7 open casing windows, with 3 extra blocked channels in one open window)

$$N = 6.5 * 4 * 7 - 3 = 179,$$

the volume flow at the outlet can then be approximated as

$$V_{out,exp} = N \times U_{ave,rad} \times A_{ch} \quad (5)$$

and is found to be  $V_{out,exp} \approx 0.089(\text{m}^3/\text{s})$ , which is close to the approximated value at the inlet,  $V_{in,exp}$ , with a difference of less than 5%.

The experimental results for almost all available channels in Figure 13 show regions of zero velocities, which refers to recirculation zones at the outlet. This is because the velocities in the recirculation regions are reversed. Comparing the experimental and the numerical results shows that the numerically computed velocity magnitudes at the outlet of the generator are of the same order of magnitude as those experimentally measured at the same place. The distribution of the numerical velocities, however, differs from the measurements. The experimental results show obvious recirculation zones on the left hand side of almost all channels,

while the numerical results show much more uniform velocity distributions in the channels.

## CONCLUSIONS

The air flow inside a small-scale electric generator has been numerically and experimentally investigated. Many geometrical details have been included in the numerical studies, while the air blockage at the outlet of the generator is different in the two cases. The larger flow blockage in the experimental rig is unavoidable due to the installation layout of the rig, and has led to uncertainties in the results. The qualitative experimental flow visualizations show good agreements with the numerical results. The quantitative experimental results, however, show less agreement with the numerical computations. The deviation of the experimental and the numerical results may be associated to different factors. An important explanation is that the flow blockages in the two cases are different, which means that the geometries are not identical. The numerical case has been run in steady-state, which is a simplified approximation to the unsteady nature of the flow.

## ACKNOWLEDGEMENTS

The research presented was carried out as a part of the "Swedish Hydropower Centre - SVC". SVC has been established by the Swedish Energy Agency, Elforsk and Svenska Kraftnät together with Luleå University of Technology, The Royal Institute of Technology, Chalmers University of Technology and Uppsala University, [www.svc.nu](http://www.svc.nu). The computational time, hardware and facilities were provided by C3SE, center for scientific and technical computing at Chalmers University of Technology in Gothenburg, Sweden, and SNIC, Swedish National Infrastructure for Computing. The authors would like to acknowledge the contribution of the VG Power electric generator manufacturer, especially Mr. Tage Carlsson, as well as Vattenfall Research and Development (VRD) for their continuous support and guidance. The access and the geometrical modifications to the generator rig at Uppsala University were provided by Mr. Mattias Wallin and Dr. Urban Lundin and is hereby acknowledged. The measurements have been performed with help of Dr. Mohsen Jahanmiri and is acknowledged here.

## REFERENCES

- [1] Moradnia, P., and Nilsson, H., CFD of air flow in hydro power generators for convective cooling, using OpenFOAM, *Proceedings of the 5th European Conference on Computational Fluid Dynamics (ECCOMAS CFD 2010), Portugal*, June 2010.
- [2] Moradnia, P., CFD of air flow in hydro power generators, Thesis for licentiate of engineering no. 2010:11, ISSN 1652-8565, Chalmers University of Technology, Sweden, December 2010.
- [3] Houde, S., Hudon, C., and Vincent, P.B., Simulation strategies of the cooling flow for large hydro-generator, *Hydro 2008, Slovenia*, 2008.
- [4] Petit, O., Page, M., Beaudoin, M., and Nilsson, H., The ERCOFTAC centrifugal pump OpenFOAM case study,

International meeting of the workgroup on cavitation and dynamic problems in hydraulic machinery and systems, 2009.

[5] Launder B. E. and Sharma B. I., Application of the energy dissipation model of turbulence to the calculation of flow near a spinning disc, *Lett. Heat Mass Transfer* **1** 131–8, 1974.